Photonic Sensing and Characterisation of Multiphase Water Flows
Computational Sensing and Imaging

Sergio L. Carrasco-Ortiz, Eduardo Valero, Maria Morant and Roberto Llorente

Nanophotonics Technology Center, Universitat Politècnica de València, Camino de Vera s/n, Valencia, Spain

Keywords: Computational Sensing, Photonic Sensor, Imaging, CMOS, Multiphase Water Flow, Cavitation, Air Fraction, Bubble Speed.

Abstract: This paper presents and demonstrates experimentally a photonic sensor based on laser excitation and CMOS array detection of light interactions in a bubbling water column. Bubbling water columns are multiphase water flows, which can be produced by cavitation effect in screws and pump-jets, or by water-air mixing in the dam intakes and spillways in hydroelectric energy generation plants. The proposed optical sensor comprises a CMOS array with a polymeric tuneable optical lens sampling the area illuminated by a diode laser operating at 532 nm. By computational imaging, the sensor is able to measure the size, shape and speed of the bubbles inside the water column and the corresponding bubble concentration. The developed laser-assisted sensor is demonstrated experimentally in the laboratory with a water column at 0.05 MPa with good results employing Optical Flow, SIFT and SURF computational methods.

1 INTRODUCTION

Bubble detection and multiphase flow monitoring are important in terms of efficiency and safety in many industrial and medical fields. A multiphase flow is defined as a simultaneous flux of two phases or components with an explicit interface between them (Iyer, et al., 2013). A basic example of a two-phase flow usually comprises a gas and a liquid, being the most common bubble flows (Bian, et al., 2011). Bubble flows play an important role in the study of mechanism in gas/liquid two-phase flows where the bubbles behaviour are a key element when monitoring water columns in industrial applications (Bian, et al., 2011). Some application examples of two-phase flows are air bubbles found in extracorporeal blood circuits of haemodialysis (Li, et al., 2015) or in industrial bubble column reactors (Iyer, et al., 2013). In the first example, in medical applications, if a certain amount of air is pumped into the patient, it may cause life-threatening coagulation and haematomas (Li, et al., 2015). In the second example, it is extremely important to know the properties of the bubbles including its size, shape and velocity for the design and function monitoring of industrial reactors (Iyer, et al., 2013). In both cases, image processing of bubbles has been proposed to calculate the number of bubbles and cumulative volume (Jonsson, 2014) (Muddle, et al., 1994).

A large number of bubbles in a flow can indicate the presence of cavitation in hydraulic applications. Cavitation is due to the pressure decrease generated by an excessive blade angular velocity, which in turn generates bubbles that explode in the blade surface (Brennen, 2005). Cavitation spaces are usually involved in highly turbulent flows as it happens in vortex emissions produced in the torch effect represented in Figure 1(a). Bubble explosion causes erosion on the surface of dam spillways, reducing its useful life (ETH Zurich, Laboratory of Hydraulics, Hydrology and Glaciology, s.f.) as it is depicted in Figure 1(b).
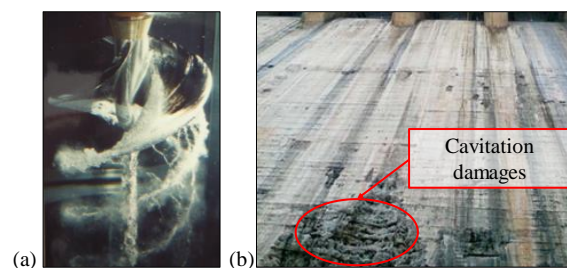

Figure 1: (a) Torch effect in a screw (b) Cavitation damage on spillway profile of Nagarjunasagar Dam.
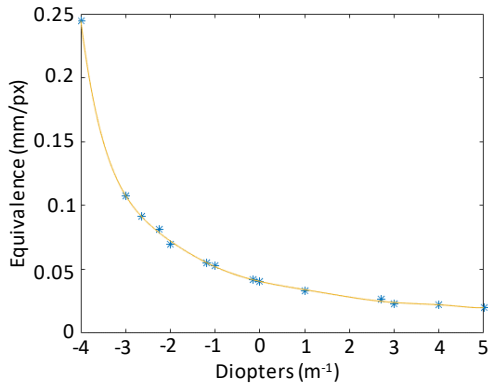
55

Furthermore, in devices such as pumps, hydraulic turbines, pump-jets and screws in the naval area (installed on ships and submarines), cavitation could cause noise, vibration, permanent screw damage and propulsion efficiency losses (Buckland, et al., 2013) (Shan-Yong, et al., 2013). In this paper, we focus on the detection (sensing) and characterization of bubbles in a multiphase flow water column. A potentially high bubble-density is considered in order to address scenarios including cavitation in marine screws, and water-air mix in hydroelectric energy generation structures.

Due to the compressibility of bubble flows, air is capable of absorbing, until a certain point, the impact of bubble shocks in cavitation processes (Peterka, 1983). However, if the bubble flow is not monitored properly it can lead to the above mentioned damages in the structure as represented in the example depicted in Figure 1(b). The aeration of the flow changes its dissipative behaviour –as provides less friction with the contours and increased vorticity– (Chanson, 1994), which converts the concentration of air in a variable of crucial interest. The level of bubble concentration modifies the macroscopic properties of the flow, increasing its draft and decreasing its velocity and gives rise to different momentum distributions relative to those of the exclusively liquid flow. In addition, significant differences have been found in the behaviour of the turbulence due to the effect of the dispersed phase (air in this case) on the carrier phase (water).

The most common solution to cavitation in hydraulic structures is the design of hydro-dynamic profiles that avoid big pressure gradients (Edel, 1977) (Volkart & Rutschmann, 1984). However, as it is not always possible and cavitation may occur at relatively slow speeds, other sort of solutions are necessary. The employment of coating materials have been also proposed in the past to improve the resistant properties (Cheng, et al., 1990). Accoustic detection of the cavitation bubbles implosion has been also evaluated in the literature (Duraiswami, et al., 1998), where incipient cavitation is heard as intermittent crackling while severe cavitation becomes a steady hiss increasing in volume (Chudina, 2003) (Karassik & McGuire, 1997). However, due to the chaotic rise of the bubbles along the flow in both number and size, it is not possible to predict the emitted noise to get a full characterization (Chudina, 2003). Other techniques for characterizing bubbles are based on energy measurement –employing charge-coupled devices (CCD) or hydrophones (Brujan, et al., 2002)– or electric impedance measurement (O'hern, et al., 1995), or using probes to measure if there is air or

water in contact with the probe (Chanson, 1997). All these methods are invasive and they will modify the hydrodynamic multiphase flow properties, such as bubble shape and flow. To avoid this, we propose a photonic sensor based on a camera and a diode laser detection that does not interfere with the flow. The diode laser is employed to excite the bubbling water column in order to increase the contrast of a high-density number of bubbles in the flow. This non-invasive method enables monitoring the flow behaviour taking high-speed images of the flow. With the proposed post-processing algorithms, from these images we can calculate the bubble speed and extract the size (bubble concentration) and shape of the bubbles in terms of equivalent area and diameter, major half-axis, minor half-axis and perimeter.

2 LASER-CMOS SENSOR ARCHITECTURE

2.1 Photonic Subsystems

Figure 2 represents the conceptual scheme of the laboratory setup including the block diagram of the main components comprising the proposed photonic sensor for the detection and characterization of bubbles in a multiphase flow. At the laboratory the sensor is applied to a bubbly water column generated -inside a transparent tank- with a cylindrical diffusor with main characteristics of diameter $\emptyset_{diff} = 12.10$ mm and length $L_{diff} = 26.50$ mm. This cylindrical diffusor is connected with a flexible plastic tube ($\emptyset_{in} = 5.10$ mm, $\emptyset_{out} = 8.10$ mm) to a void pump configured with 0.05 MPa.

The laser-assisted sensor is based on a camera that comprises a complementary metal-oxide-semiconductor (CMOS) sensor, a fixed lens and a tunable lens controlled remotely with a driver. The illumination of the bubbles is achieved with a laser diode beam dispersed by a negative lens.

Figure 2: Conceptual scheme of the laser-assisted CMOS sensor developed at the laboratory.

Figure 3: Tunable lens and fixed lens system's calibration curve for the equivalence of mm/px vs. dioptres.

The main functions of each opto-electronic component depicted in Figure 2 are:

- Monochrome CMOS sensor, responsible for the acquisition of data: A camera with CMOS sensor was selected because it is the fastest and safest way to capture optical information in form of images. The sensor is configured remotely in terms of resolution, exposure time, gain, frames per second (fps) and recording time. In these experiments, we used a sensor with a maximum resolution of 1280×1024 pixels (px).
- Fixed lens with a focal length of $f = 25$ mm, responsible for focusing the image together with a tunable lens.
- Tunable lens, responsible for adjusting the lens system: At the fixed lens outer face a tunable lens is used. This lens is capable of varying its dioptre number between −4 and 5 dpt to focus in different depth planes.
- The lens system is controlled by algorithms that set the tunable lens' dpt. This is necessary for the calculation of real lengths. The algorithms calculate the equivalence between the image size in terms of px and the real length in mm. Figure 3 shows the calibration curve of the lens system in terms of mm/px vs. dioptres. In this work the refractive surface between the two media (air and water) is plane, and by the Snell's law, it is obtained an increase factor m = 1; meaning that there is no sizing increase due to the refraction. Applying in Figure 3 a polynomial adjustment of 8th degree, the equivalence is given by the equation (1) being their coefficients those written in Table 1:

$$Eq = \sum_{k=0}^{8} C_k \cdot dpt^k \qquad (1)$$

Table 1: Equation (1) coefficients.

C_0	0.0405
C_1	-8.007e-3
C_2	2.618e-3
C_3	-1.098e-3
C_4	-7.327e-5
C_5	1.218e-4
C_6	2.537e-6
C_7	-8.161e-6
C_8	9.07e-7

The equivalence defined in equation (1) is included in the processing algorithms to calculate the equivalence between px and millimetres for each measurement. Without this calibration, we would be unable to transform the pixels obtained in the post-processing step into millimetres.

- The laser diode, responsible for illuminating the bubbles and increase the contrast and shadowing of the borders. A tunable output power laser with up to 80 mW working at a wavelength of $\lambda = 532$ nm is used. The concrete wavelength was selected to match the quantum efficiency of the CMOS sensor. Figure 4 shows the efficiency of the CMOS sensor used for different wavelengths. The quantic efficiency of the CMOS sensor is over 68% for a $\lambda = 532$ nm. The geometrical laser ray has a roundness $O > 90$ %, divergence $\theta > 1.2$ mrad and initial diameter $\emptyset_0 = 1.5$ mm. The output power of the laser can be configured depending on the voltage/intensity provided ranging from 2.3 to 2.9 V and up to 350 mA. In these experiments, we waited ten seconds after switching on the laser in order to ensure the output power.
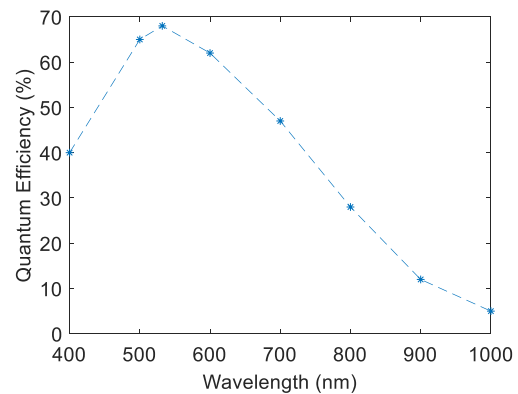
Figure 4: CMOS quantum efficiency.

- Negative (divergent) lens, responsible for enlarging the laser beam. In order to avoid the appearance of sparkles in the image produced by the CMOS sensor it is necessary to diverge the laser beam. To achieve it, a negative NBK-7 glass lens with plane-concave shape is used with a focal distance $f = -75$ mm, diameter of $\emptyset = 50.8$ mm.

2.2 Data Acquisition and Digital Signal Processing

Figure 5 depicts the main steps followed for the data acquisition and processing of the images to full characterize the bubble flow.. As a first step, the sensor is configured remotely via C commands including the CMOS configuration, the output power of the laser diode and the lens focus. The CMOS sensor is configured in:

- Gain correction, employed to homogenise the CMOS sensibility. The dead pixel correction allows the software to fix the turned off pixels. This correction consists in storing the average value of the adjacent pixels in the black pixel. Furthermore, it is useful to post-process the images as improves the detection area, but at the same time, may cause errors in the image's adaptive histogram equalisation.
- Exposure time, also known as shutter speed, adjusts the amount of incident light in order to avoid blurred images.
- Recording speed: Readout speed tells how many frames-per-second the camera can capture. In these experiments, after capturing the images at a speed of 100 fps (i.e. each frame is captured at 1/100 seconds or 10 ms), the speed is immediately set to 1110 fps (i.e. 1/1110 or 0.9 ms) reducing the region of interest (RoI). This greatly improves the result of bubble speed estimation.

Once the image sequence is recorded, adjusting the focus system, the equivalence value is obtained with the mm/px conversion depicted previously in Figure 3. In the image-processing step, the recognition of any object is carried out by the discrimination of what is seen regarding the ideal concept of the object to be identified. To achieve that, it is necessary to transform the images acquired in greyscale –pixels whose values go from 0 to 1, being 0 a black pixel and being 1 a white pixel– into images in which there are just black and white pixels. This process is known as binarization as only 0 or 1 values remain in the image.
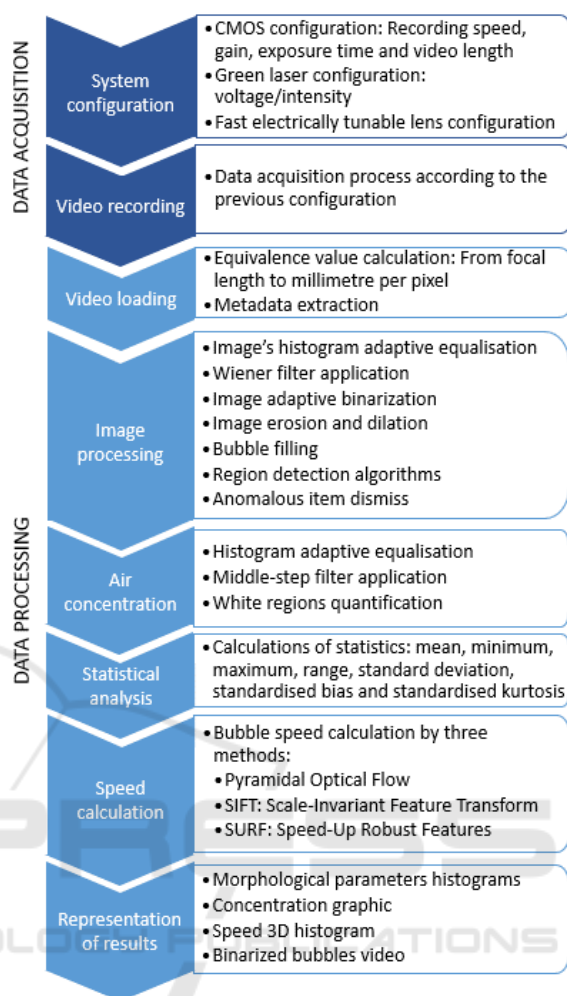
Figure 5: Data acquisition and processing diagram.

To minimize the interclass variance between the white and black pixels, it is necessary to have some ambient lighting. An accurate conversion from a grey image to a binarized image is essential for the application of region detection algorithms. The laser diode illumination provided by our optical sensor increases the contrast of the bubbles in the flow and enhances the binarization process.

In order to carry out the identification of circular/elliptical forms some extra filtering and processing should be implemented to the images, as depicted in Figure 6.
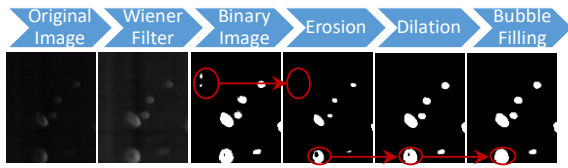
Figure 6: Evolution of an image captured from the water column after digital signal processing.

The filters and processes applied to the images are integrated in C/Fortran language. Figure 6 shows the different steps applied to the images captured from the water column including:

- Wiener filter (Bankman, 2008): provides a statistical computation from a degraded image. This filter is designed considering that the image and its noise are random processes.
- Image erosion: This function erodes the binary image applying a structuring element object in order to erase the remaining noise after the Wiener filter.
- Image dilation: Due to the previous image erosion, in some cases it is necessary to recover lost white pixels as it can be observed in Figure 6. In order to do so, a dilatation of the image is implemented employing the same structuring element object applied previously in the erosion step.
- Bubble filling: In order to be able to employ properly the region detection algorithms, we explore the binary image as a matrix composed by ones and zeros. The filling algorithms locate those 0 pixels in the matrix surrounded by ones and replaces the 0 within by 1, filling the bubble contour.
- Anomalous item dismiss: In the sensing area, two or more bubble may appear too close each other, providing mistakes in the statistical analysis of the bubble shape. To avoid this, data with 1.5 times higher the morphological bubble parameters typical deviation, was debugged from the analysis.

After the statistical analysis of the detected bubbles, the bubbles' speed is calculated. In this topic, we performed an exhaustive state-of-the-art study of the methods available for the calculation of the velocity profile of moving objects. In particular, in these experiments we compare three evaluation methods:

- Optical Flow, based on the distribution of apparent velocities of brightness movement patterns. Pyramidal optical flow arises from the relative movement of objects and the observer,

so it does not take into account the movement of the observer (Horn & Schunck, 1981).
- Scale-Invariant Feature Transform (SIFT) (Lowe, 2004), which computing steps are scale-space extrema detection, key-point localization, orientation assignment and key-point descriptor. This method identifies key-points in a set of images in order to compare later every new image with an older one to find matching features based on the Euclidean distance of their feature vectors.
- Speed-Up Robust Features (SURF) (Bay, et al., 2008): This method searches for patterns in the recognized points in discrete images classified in three types, i.e. points of interest, descriptors and markers.

Once the bubbles' speed is calculated, the processing algorithms represent the results in form of histograms and saves the binarized video for further evaluation.

3 EXPERIMENTAL BUBBLE CHARACTERIZATION RESULTS

The validation of the developed processing algorithms using the proposed sensor is performed at the laboratory with bubbly water columns within a transparent tank as depicted previously in Figure 2. In these experiments, the void pump was set to 0.05 MPa to generate a turbulent bubbly flow with similar bubble shapes and sizes.

3.1 Air Bubble Concentration Calculation

The air bubble concentration, i.e. the air in the form of bubbles in the sensed area, is carried out integrating all the white regions detected after the binarization of the image. Figure 7(a) shows the raw image acquired by the sensor and Figure 7(b) shows the binarized image result for bubble concentration calculation. In the processed representation, the background was coloured in green to enhance the contrast of the results.

As it can be observed in Figure 7(b), for the concentration calculation we do not dismiss any anomalous form, as the clusters of bubbles are also taken into account for the total concentration in the area. In these experiments, the bubble concentration is evaluated in every frame acquired (i.e. 500 frames).
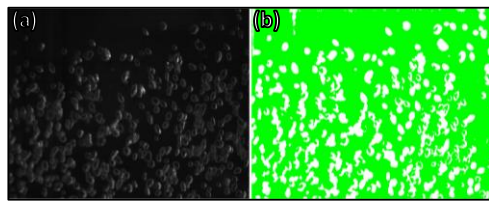
Figure 7: (a) Original frame vs. (b) binarized frame sample for the calculation of bubble concentration.

Figure 8 shows the experimental mean of bubble concentration measured in an area of 53.67 cm^2 (81.92 mm $\times$ 65.52 mm), during 5 s for 500 images.
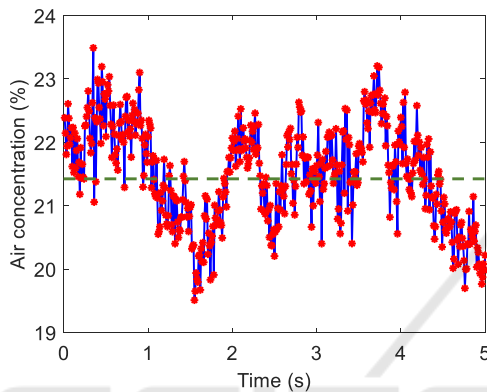

Figure 8: Experimental results of bubble concentration analysis. Horizontal line indicated the mean of bubble concentration in the detected area of 21.5%.

In this example, the measured bubble concentration mean is 21.5%, ranging from 19.51% to 23.49% in a sensed period of 5 seconds. Figure 8 represent in the red marks the bubble concentration for each frame and in blue lines the slope between sequential frames.

3.2 Bubbles' Shape

As it was described in detail in Section 2.2, applying region detection algorithms to the binarized images, we were able to quantify shape parameters in the white regions –filled bubbles–. From the filtered data, region detection algorithms are able to calculate the bubbles' shape parameters, e.g. equivalent area and both half-axes. The typical deviation (σ) for each parameter is calculated to debug data what surpass 1.5 times its σ. This debugging is intended to remove the bubbles that, being too close each other, appeared as one bigger bubble after binarization. Figure 9 compares the acquired data with the processed image after binarization, filtering and debugging. The processing algorithms are applied to the same original raw data as in Figure 7 so, comparing both figures,

we can observe the debugging of bubble clusters and anomalous items for the analysis of bubbles' shapes.
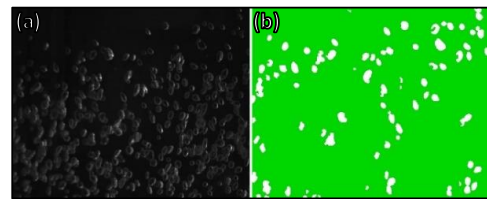
Figure 9: (a) Original frame vs. (b) processed frame sample for the statistical analysis of bubbles' shapes.
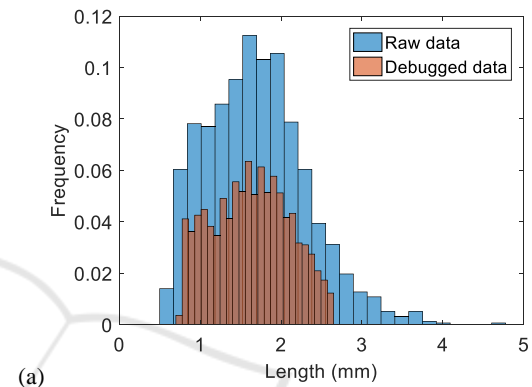

(a)

(b)
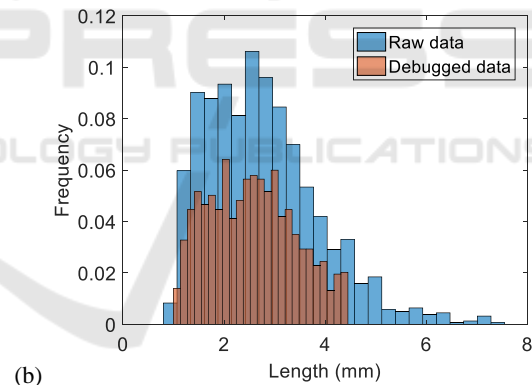
Figure 10: Histogram of the experimental results for (a) minor and (b) major half-axis estimation (raw vs. debugged data) expressed as parts per unit.

Figure 10, shows the experimental results for minor and major half-axis. The mode of the minor and major half-axis is 1.67 mm and 2.04, respectively, as observed in Figure 10(a) and (b). It is clearly observed that the debugging of anomalous items eliminates clusters of half-axis bigger than 2.63 mm (minor half-axis) and larger than 4.44 mm (major half-axis).
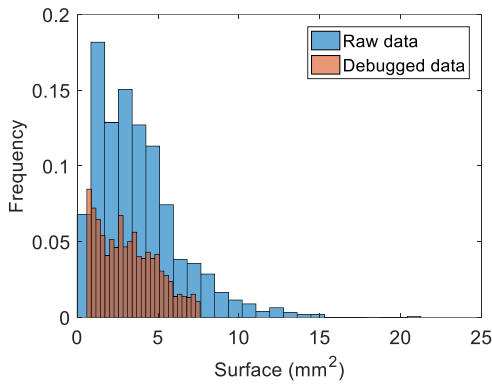
Figure 11: Histogram of the experimental results for equivalent area estimation (raw vs. debugged data) expressed as parts per unit.

Figure 11 shows the statistical results for equivalent area of the bubbles present in the water column. The mode of the equivalent area is 0.66 mm^2, being the maximum equivalent area found by the algorithms after the debugging of anomalous items 7.55 mm^2.

By means of statistical analysis of data associated with bubbles such as mode, mean ($\bar{x}$), minimum (Min), maximum (Max) and σ; the measurement of the fraction of air and bubble shape in critical multiphase flows in electricity generation facilities is carried out. Table 2 summarizes the statistical analysis results obtained with debugged data. From the analysis of the experimental bubbly water column, the minor and major half-axis has a mean of 1.64 and 2.57 mm, respectively. The mean equivalent area of the bubbles is of 3.19 mm^2 with a deviation of $\sigma = 1.78$. This deviation appears due to the non-uniform porous diameter of the diffusor that generates bubbles with different sizes as expected in a real-case hydraulic scenario.

Table 2: Statistical analysis with debugged data.

Parameter	Mode	$\bar{x}$	Min	Max	σ
Minor half-axis (mm)	1.67	1.64	0.78	2.63	0.47
Major half-axis (mm)	2.04	2.57	1.10	4.44	0.85
Eq. area (mm^2)	0.66	3.19	0.64	7.55	1.78

3.3 Bubbles' Speed Calculation

Figure 12 represents the 3D histograms of the bubble speed distribution in bubbly water column calculated with different estimation methods. The mean and the mode of speed results represented in Figure 12 are summarised in Table 3. It can be observed that all the speed estimation algorithms (Optical Flow, SIFT and SURF) have a mode of 0.4 m/s. The SIFT estimation has a mean slightly higher than Optical Flow and SURF methods but only in a 5%.
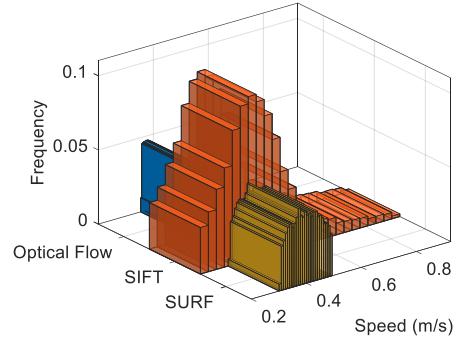

Figure 12: Bubbles' speed estimation calculated with different algorithms expressed as parts per unit.

Table 3: Bubbles' speed statistical results for different estimation methods.

Method	Mean	Mode
Optical Flow	0.40 m/s	0.40 m/s
SIFT	0.42 m/s	0.40 m/s
SURF	0.40 m/s	0.40 m/s

4 CONCLUSIONS

We propose and demonstrate experimentally a photonic sensor comprising a laser diode and a CMOS array with tunable optic lens designed to calculate the size and speed of the bubbles present in a bubbly water column. With this information, it is possible to increase efficiency and security in power generation plants while ensuring a longer duration of the usefulness not only of the structure but also of the hydraulic components, such as turbines and screws.

In this work, we presented proposed laser-assisted CMOS sensor and the associated algorithms to process the data. The optical sensor comprises a CMOS sensor that captures high-speed frames of the bubbles illuminated with a laser diode. A laser diode emitting in $\lambda = 532$ nm is selected to optimize the CMOS sensing performance.

Experimental data gathered indicates that bubble's shape depends on the diffusor porous dimensions. In these validation examples the minor and major half-axis of the bubbles are estimated to be 1.64 and 2.57 mm, respectively. The mean equivalent area of the bubbles is of 3.19 mm^2 with a deviation of

$\sigma = 1.78$. Such typical deviation appears due to the diffusor porous diameter is not uniform; generating bubbles with different sizes emulating a real-case hydraulic scenario. The experimental results point out that a correct binarization is necessary to calculate the air concentration in the sensed area. For this reason, the laser-assisted sensor increases the contrast and shape contouring of the bubbles to enhance the processing efficiency.

ACKNOWLEDGEMENTS

REFERENCES

Bankman, I., 2008. *Handbook of Medical Image Processing and Analysis.* s.l.:Academic Press.

Bay, H., Ess, A., Tuylaars, T. & Van Gool, L., 2008. Speed-Up Robust features (SURF). *Computer Vision and Image Understanding,* Junio, 110(3), pp. 346-359.

Bian, Y., Dong, F. & Wang, H., 2011. Reconstruction of Rising Bubble with Digital Image Processing Method. *Instrumentation and Measurement Technology Conference (I2MTC).*

Brennen, C. E., 2005. *Fundamentals of Multiphase Flows.* Pasadena(California): Cambridge University Press.

Brujan, E. A., Keen, G. S., Vogel, A. & Blake, J. R., 2002. The final stage of the collapse of a cavitation bubble close to a rigid boundary. *Physics of Fluids,* 14(1), pp. 85-92.

Buckland, H. C., Masters, I., Orme, J. A. C. & Baker, T., 2013. Cavitation inception and simulation in blade element momentum theory for modelling tidal stream turbine. *Part A: Journal of Power and Energy,* Junio, 227(4), pp. 479-485.

Chanson, H., 1994. Drag reduction in open channel. *Journal of Hydraulic Research,* 32(1), pp. 87-101.

Chanson, H., 1997. Air bubble entrainment in open channels. Flow structure and bubble size distributions. *Intl Jl of Multiphase Flow,* 23(1), pp. 193-203.

Cheng, C., Webster, C. & Wong, J., 1990. Cavitation-resistant coatings for concrete hydraulic structures. *ACI Materials Journal,* 87(6), pp. 594-601.

Chudina, M., 2003. Noise as an Indicator of Cavitation in a Centrifugal Pump. *Acoustical Physics,* 49(4), pp. 463-474.

Duraiswami, R., Prabhukumar, S. & Chahine, G. L., 1998. Bubble counting using an inverse acoustic scattering method. *The Journal of the Acoustical Society of America,* 104(5), pp. 2699-2717.

Edel, Y. U., 1977. Guide to protecting spillway structures from cavitation, Power Technology and Engineeringformerly Hydrotechnical Construction). *Springer,* 11(9), pp. 948-949.

ETH Zurich, Laboratory of Hydraulics, Hydrology and Glaciology, n.d. *Air detrainment of high-speed waters flows.* [Online] Available at: http:\\www.vwa.ethz.ch/ people/hy/archive/hy_151_air_detrainment [Accessed 2017 06 12].

Horn, B. K. P. & Schunck, B. G., 1981. Determining optical flow. *Artificial Intelligence,* 17(1-3), pp. 185-203.

Iyer, K., Shridharani, S., Arunkumar, S. & Venkatesan, M., 2013. Application of Image processing for a Bubble Column Reactor. *Computational Intelligence and Computing Research (ICCIC).*

Jonsson, P., 2014. Evaluation of air micro bubbles in dialysis sustems in vitro. *American Journal of Kidney Diseases,* 63(5).

Karassik, I. & McGuire, T., 1997. *Centrifugal Pumps.* 2nd ed. ed. New York: Pergamon.

Li, N., Jia, L. & Zhang, P., 2015. Detection and volume estimation of bubbles in blood circuit of hemodialysis by morphological image processing. *Cybernetics and Intelligent Systems (CIS) and IEEE Conference on Robotics, Automation and Mechatronics (RAM).*

Lowe, D. G., 2004. Distinctive Image Feature from Scale-Invariant Keypoints. *International Journal of Computer Vision,* Noviembre, 60(2), pp. 91-110.

Muddle, R. F., Schulte, H. B. M. & Vand den Akker, H. E. A., 1994. Analysis of a bubbling 2-D gas-fluidized bed using image processing. *Powder Technology,* 81(2), pp. 149-159.

O'hern, T. et al., 1995. Development of an electrical impedance tomography system for an air-water vertical water-column. *Forum on Measurement techniques in Multiphase Flowa ASME,* pp. 1-9.

Peterka, A. J., 1983. The effect of entrained air on cavitation pitting. *Proceedings of Minnesorta International Hydraulic Convention,* pp. 507-518.

Shan-Yong, L., Jiang-An, W. & Si-Guang et al., Z., 2013. Laser detection method of shi`p wake bubbles based on multiple scattering intensity and polarization characteristics.. *Acta Phys. Sin,* 62(6)(060704).

Volkart, P. & Rutschmann, P., 1984. Rapid flow in spillway chutes with and without deflectors. A model-prototype comparison. *Proceedings of the Symposium on Scale Effects in Modeling Hydrualic Research,* pp. 3-6.